Cement and
Concrete
Research

Enhanced modeling of moisture equilibrium and transport in cementitious materials under arbitrary temperature and relative humidity history

Tetsuya Ishida [a,*], Koichi Maekawa [a], Toshiharu Kishi [b]

[a] *Department of Civil Engineering, The University of Tokyo, 7-3-1 Hongo, Bunkyo-ku, Tokyo, Japan*
[b] *Institute of Industrial Science, The University of Tokyo, 4-6-1 Komaba, Meguro-ku, Tokyo, Japan*

Abstract

This paper focuses on behaviors of moisture dispersed in nano-macro scale pores under various temperature and relative humidity conditions. The authors formulated an equilibrium relationship between liquid and vapor phases and a moisture flux driven by pore pressure, vapor pressure and temperature gradients. In addition, liquid and interlayer water were measured separately by ethanol in order to reveal each temperature sensitivity in saturation-humidity paths. Based on the experiments, a modified hysteresis model for moisture isotherm was proposed. Verifications with experimental data showed that the proposed method can simulate moisture behaviors under various temperature conditions.
© 2006 Elsevier Ltd. All rights reserved.

Keywords: Transport properties; Drying; Microstructure; Diffusion; Permeability

1. Introduction

Many of the macroscopic nonlinear phenomena found in cementitious materials are attributable to the state of moisture present in both liquid and vapor forms. For example, it has been widely known that hydration reaction, shrinkage, and creep under sustained load are closely related to the moisture in concrete. In addition, moisture plays a very important role in mass transport as solvents or reaction fields of deterioration processes. Since cementitious materials are able to keep moisture stably under normal conditions, they show unique behaviors that are not seen in the case of other industrial materials. It is therefore essential to predict the water content in unsaturated porous media under any environmental condition in order to assess concrete performance.

In the past, the authors developed thermodynamic models for the hydration reaction of cement, the micro-pore structure formation, and moisture equilibrium and transport, and their system dynamics [1–3]. As modeling of moisture transport, the authors formulated the flux of both liquid and vapor driven by pore pressure and vapor density. In addition, moisture state in

the system can be obtained by combining thermodynamic theory and computed micro-pore structure. This methodology enables us to simulate the moisture profiles under arbitrary drying–wetting history. These models, however, were verified mainly at normal temperature (20 °C). This study aims to generalize a moisture transport model and a moisture equilibrium model with respect to temperature. Since real concrete structures are used under different temperature conditions, it is important, from an engineering point of view, to expand the scope of application of the model for use under arbitrary temperature and humidity conditions. The purpose of this study is to quantify the temperature sensitivity of the state and transport of moisture in nanometer to micrometer scale pores both experimentally and theoretically and enhance a system for estimating the distribution and transport of internal moisture under arbitrary temperature conditions.

2. Thermodynamic model for moisture transport and equilibrium

2.1. Governing equation for moisture in a system

The law of mass conservation governing the moisture balance in a system is expressed by Eq. (1). The accuracy and

---

applicability of the analysis system depends on modeling of each term in the equation.

$$\frac{\partial \theta_w}{\partial t} + \text{div}\,(J(\theta_w, T, \nabla \theta_w, \nabla T)) + Q = 0 \qquad (1)$$

where, θ_w: the mass of moisture in a unit volume of concrete [kg/m^3], J: moisture flux [kg/m^2 s], T: temperature [K], and Q: sink term corresponding to water consumption due to hydration [kg/m^3 s].

In the past research [1,2], the potential term (first term in Eq. (1)), which represents moisture capacity of the material, and the flux term (second term in Eq. (1)) have been verified only for normal-temperature condition (20 °C). For the purpose of widening the applicability, temperature-dependent moisture transport and equilibrium models are introduced in this chapter.

2.2. Equilibrium between liquid and vapor phases of water under arbitrary temperatures

The potential term for the moisture in a porous material can be expressed as

$$\frac{\partial \theta_w}{\partial t} = \frac{\partial (\rho_1 \phi S)}{\partial t} \qquad (2)$$

where, ρ_1: density of liquid water [kg/m^3], ϕ: porosity, and S: degree of saturation of porosity. The mass of water vapor is ignored in this term since it is negligibly small compared with that of liquid water. As well known, the density of liquid water ρ_1 is temperature-dependent. An equation derived by regression of measured values [4] is used in this study (Fig. 1).

$$\rho_1 = 1.54 \times 10^{-8} \cdot T^3 - 1.85 \times 10^{-5} \cdot T^2$$
$$+ 6.65 \times 10^{-3} \cdot T + 2.47 \times 10^{-1} \qquad (3)$$
$$(273 < T < 373)$$

In order to compute the degree of saturation S, it is necessary to describe the relationship between the liquid water and water vapor in the pores. Liquid water in the microstructure is always
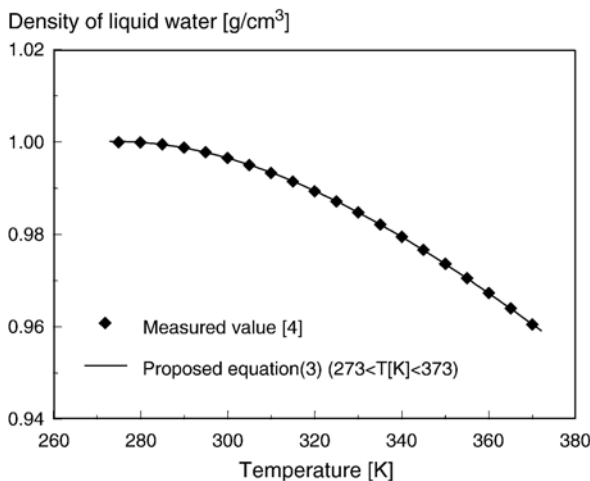
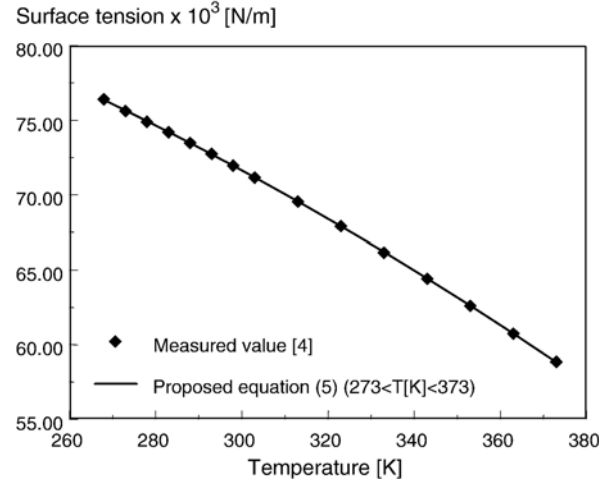Fig. 1. Relationship between temperature and density of liquid water.

Fig. 2. Relationship between temperature and surface tension of liquid water.

under negative pressure P_1 [Pa] due to its surface tension. By assuming that a pore is cylindrical, a relationship between this pressure and the surface tension γ of liquid water can be calculated from the following equation as [1,2]

$$P_1 = -\frac{2\gamma}{r} \qquad (4)$$

where, r: pore radius [m], and γ: surface tension of liquid water [N/m]. Since the surface tension of liquid water also varies with temperature, an equation derived by regression of measured values [4] is used similar to the density of liquid water (Fig. 2).

$$\gamma(T) = 2.66 \times 10^{-4} \cdot T^2 + 3.17 \times 10^{-3} \cdot T$$
$$+ 9.46 \times 10^1 \qquad (273 < T < 373) \qquad (5)$$

Absolute vapor pressure p_{vap} [Pa] in the pores becomes lower than that in the atmosphere due to formation of meniscus. In a state of phase equilibrium, the Gibbs free energy in the gas and liquid phases are equal, so the following relation is obtained:

$$RT \ln \frac{p_{\text{vap}}}{p^*} = V_1 \cdot P_1 \qquad (6)$$

where, R: gas constant [J/mol K]; p^*: saturated vapor pressure [Pa], and V_1: molar volume of liquid water [m^3/mol]. The ratio p^*/p_{vap} corresponds to relative humidity. Substituting $V_1 = M_w/\rho_1$ by using the molar volume M_w [kg/mol] and density ρ_1 [kg/m^3] of liquid water and rewriting finally gives,

$$P_1 = \frac{\rho_1 RT}{M_w} \ln \frac{p_{\text{vap}}}{p^*} \qquad (7)$$

where, the saturated water vapor pressure, p^*, varies with temperature. The value of p^* at an arbitrary temperature can be calculated from the Clausius–Clapeyron equation:

$$\frac{d \ln p}{dT} = \frac{\Delta H_{\text{vap}}}{RT^2} \qquad (8)$$

where, ΔH_{vap} is the heat of evaporation [kJ/mol] of liquid water. If the range of temperatures to which the proposed model is

applicable is 273 [K] to 373 [K], the heat of evaporation of liquid water may be considered to be almost constant regardless of temperature. Therefore, integrating Eq. (8) assuming that the heat of evaporation gives,

$$
\begin{aligned}
p_{vap} &= p^* \exp\left(\frac{P_l M_w}{\rho_l RT}\right) \\
&= p_0 \exp\left\{-\left(\frac{\Delta H_{vap}}{R}\right)\left(\frac{1}{T} - \frac{1}{T_0}\right)\right\} \exp\left(\frac{P_l M_w}{\rho_l RT}\right)
\end{aligned}
\tag{9}
$$

where, p_0 and T_0 are reference pressure and reference temperature, respectively.

2.3. Modeling of moisture flux in a system

In order to generalize the modeling of moisture flux with respect to temperature, a flow driven by both the pore pressure gradient and the temperature gradient is considered. In this case, the moisture flux J [kg/m^2 s] for both vapor and liquid water can generally be expressed as,

$$
J = -\left(D_p \nabla P_l + D_T \nabla T\right)
\tag{10}
$$

where, D_p: moisture conductivity [kg/Pa m s] with respect to the pore pressure gradient, and D_T: moisture conductivity [kg/K m s] with respect to the temperature gradient.

A conventional vapor transport model [1] applicable to the isothermal condition formulates the flux q_v [kg/m^2 s] driven by the relative humidity gradient as follows:

$$
q_v = -\frac{\rho_v^{sat} \phi D_0}{\Omega} \int_{r_c}^{\infty} \frac{dV}{1 + N_k} \nabla h
$$
$$
N_k = \frac{l_m}{2(r - t_a)}
\tag{11}
$$

where, ρ_v^{sat}: saturated vapor density [kg/m^3], D_0: vapor diffusivity [m^2/s] in free atmosphere at 293 [K], Ω: parameter representing tortuosity of pore ($= (\pi/2)^2$), r_c: pore radius at which an interface between liquid and vapor is created, N_k: Knudsen number; l_m: mean free path of gas molecules [m], V: normalized pore volume, h: relative humidity, and t_a: thickness [m] of an adsorbed layer in a pore, calculated by using the modified B.E.T. theory proposed by Hillerborg [5]. According to this theory, the adsorbed layer thickness t_a can be calculated from Eq. (12):

$$
t_a = \frac{0.525 \times 10^{-8} h}{(1 - h/h_m)(1 - h/h_m + 15h)}
\tag{12}
$$

where, h_m: relative humidity required for completely filling the pore with liquid water. The value of h_m can be calculated, from the conditions for thermodynamic equilibrium defined by Eqs. (4) to (9), as follows:

$$
h_m = \exp\left(\frac{-\gamma M_w}{\rho_l RT r_1}\right)
\tag{13}
$$

where r_1 is a value [m] obtained by subtracting the adsorbed layer thickness from the pore radius.

When dealing with vapor flow under various temperature conditions, the gradient of relative humidity cannot be defined as transport potential. In other words, relative humidity at different temperatures does not represent the driving force correctly, since the saturated vapor pressure depends on temperature, which leads to different relative humidity even though vapor density of the system is same. Eq. (11), therefore, is generalized as shown below in order to apply it to arbitrary temperature conditions.

$$
q_v = -\frac{\phi D_0(T)}{\Omega} \int_{r_c}^{\infty} \frac{dV}{1 + N_k} \nabla \rho_v = -D_v \nabla \rho_v
$$
$$
N_k = \frac{l_m}{2(r - t_a)}
\tag{14}
$$

where, D_v: vapor diffusivity in concrete [m^2/s]. The proposed vapor transport model is driven by the gradient of absolute vapor density ρ_v [kg/m^3] in the system. The product of the relative humidity h and ρ_v^{sat} in Eq. (11) corresponds to this ρ_v. Under an isothermal condition, therefore, Eq. (14) is equivalent to Eq. (11). The vapor diffusivity D_0 in free space is dependent on temperature, so it is calculated from Eq. (15) [6]:

$$
\frac{D_0(T_1)}{D_0(T_2)} = \left(\frac{T_1}{T_2}\right)^{3/2} \left(\frac{\Omega_{D,T_2}}{\Omega_{D,T_1}}\right)
\tag{15}
$$

where, Ω_D: collision integral at temperature T_1 or T_2, given as a function of Boltzmann constant ($= 1.38 \times 10^{-23}$ [J/K]), temperature, and so on.

Next, a formula for liquid water transport is derived. The flux of liquid water q_1 [kg/m^2 s] can be calculated using the following model:

$$
q_1 = -\frac{\rho_l \phi^2}{50\eta} \left(\int_0^{r_c} r dV\right)^2 \nabla P_l = -K_l \nabla P_l
\tag{16}
$$

where, K_l: liquid conductivity [kg/Pa m s]. From the viewpoint of temperature changes, the most significant factor affecting liquid water transport is the viscosity η [Pa s] of liquid water. The viscosity η is expressed as

$$
\eta = \eta_i \exp\left(\frac{G_e}{RT}\right)
\tag{17}
$$

where, η_i: viscosity of liquid water under ideal conditions, and G_e: additional Gibbs energy required for liquid flow under non-ideal conditions. Because the viscosity η_i of liquid water, like density and surface tension, is dependent on temperature, the following regression formula based on measured values [4] is used (Fig. 3):

$$
\begin{aligned}
\eta_i =\ & 3.38 \times 10^{-8} \cdot T^4 - 4.63 \times 10^{-5} \cdot T^3 \\
& + 2.37 \times 10^{-2} \cdot T^2 + 5.45 \cdot T + 4.70 \times 10^2 \\
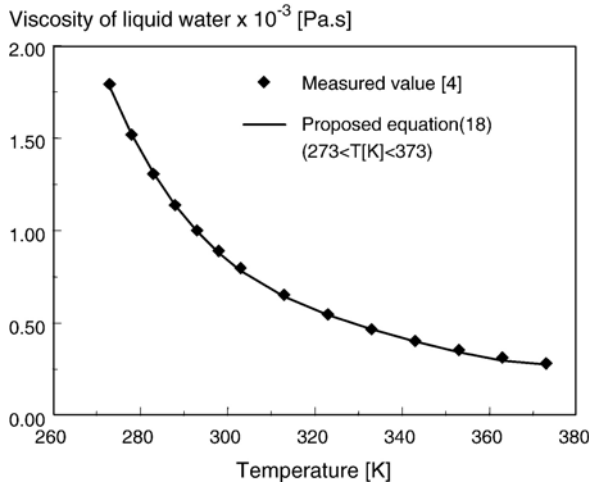& (273 < T < 373)
\end{aligned}
\tag{18}
$$

Fig. 3. Relationship between temperature and viscosity of liquid water.

From above, the moisture fluxes can be summarized as shown in Eq. (19):

$$
\begin{aligned}
J &= -(D_v \nabla \rho_v + K_1 \nabla P_1 + K_T \nabla T) \\
&= -\left\{ D_v \left(\frac{\partial \rho_v}{\partial P_1} \nabla P_1 + \frac{\partial \rho_v}{\partial T} \nabla T \right) + K_1 \nabla P_1 + K_T \nabla T \right\} \\
&= -\left(D_v \frac{\partial \rho_v}{\partial P_1} + K_1 \right) \nabla P_1 - \left(D_v \frac{\partial \rho_v}{\partial T} + K_T \right) \nabla T \\
&= -(D_p \nabla P_1 + D_T \nabla T)
\end{aligned}
\tag{19}
$$

The term expressed as $K_T \nabla T$ in Eq. (19) represents thermal diffusion known as the Soret effect [6]. For the sake of simplicity, thermal diffusion (Soret effect) is ignored ($K_T \approx 0$) since the contribution of thermal diffusion to the total flux is not well known, and this phenomenon normally plays a minor role in diffusion compared with moisture transfer driven by pore pressure and vapor pressure gradient [6].

2.4. Calculation of the degree of saturation in porous system

The relationships among pore pressure, saturated vapor pressure and absolute vapor pressure at arbitrary temperatures have been obtained through the formulation described in Section 2.2. As in the conventional model, distribution of liquid water in pores can be determined by combining these thermodynamic conditions with the geometric characteristic of the micro-pore structures. Depending on the size of pores in which water exists, however, it may be necessary to take into consideration the possibility of different states of equilibrium of water. Thus, it is reasonable to infer that condensed liquid water existing in spaces of nanometer to micrometer dimensions, water adsorbed onto wall surfaces, and interlayer water [7] in which the behavior of individual molecules is conspicuous have different sensitivity to temperature and humidity.

On the basis of this inference, the authors classified water existing in pores into capillary, gel and interlayer water, and developed different physical models corresponding to the pore sizes and states of these types of water [1–3] (Figs. 4 and 5). Water existing in gel and capillary pores ranging in size from nanometers to micrometers is calculated as condensed liquid water and adsorbed water according to thermodynamic theory. The hysteresis behavior is estimated by taking into account the inkbottle effect. For interlayer water, detailed behavior in very fine spaces corresponding to the size of individual molecules has not yet been made clear. Then, a macroscopic model is used in numerical analyses as a first approximation [1,2].

By combining existing multi-scale models for water (Figs. 4 and 5) and the moisture equilibrium equations proposed in Section 2.2 of this chapter (Eqs. (4) and (7)), the authors tried to compute moisture isotherms at 20 °C and 60 °C. When the degree of saturation in gel pores and capillary pores is calculated, it is assumed that all pores whose radii are smaller than the radius r_c in which a vapor–liquid interface is created are filled with condensed water. The saturation S_c by such
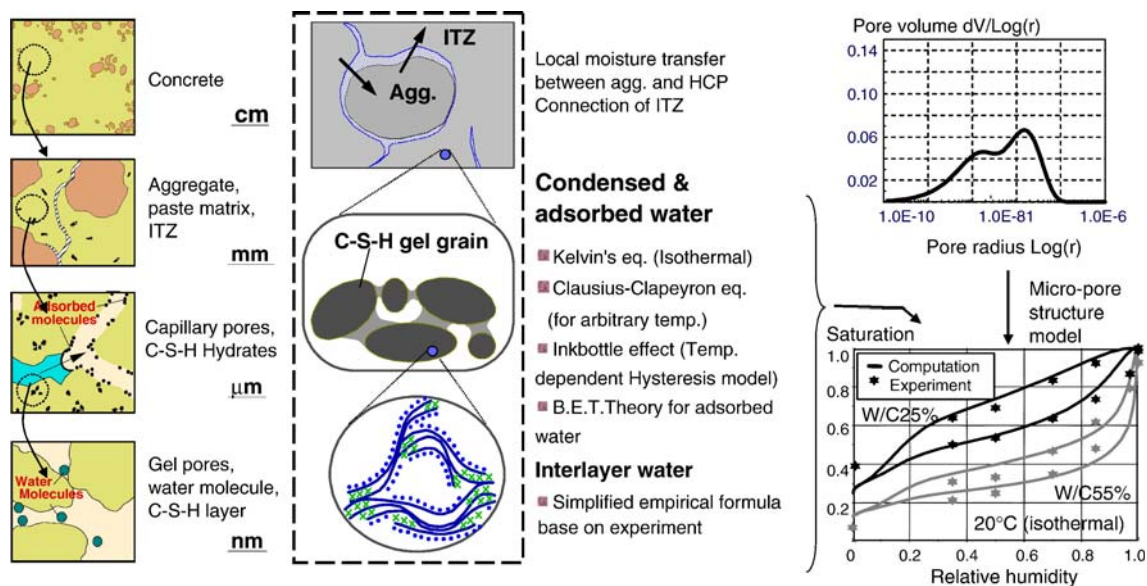

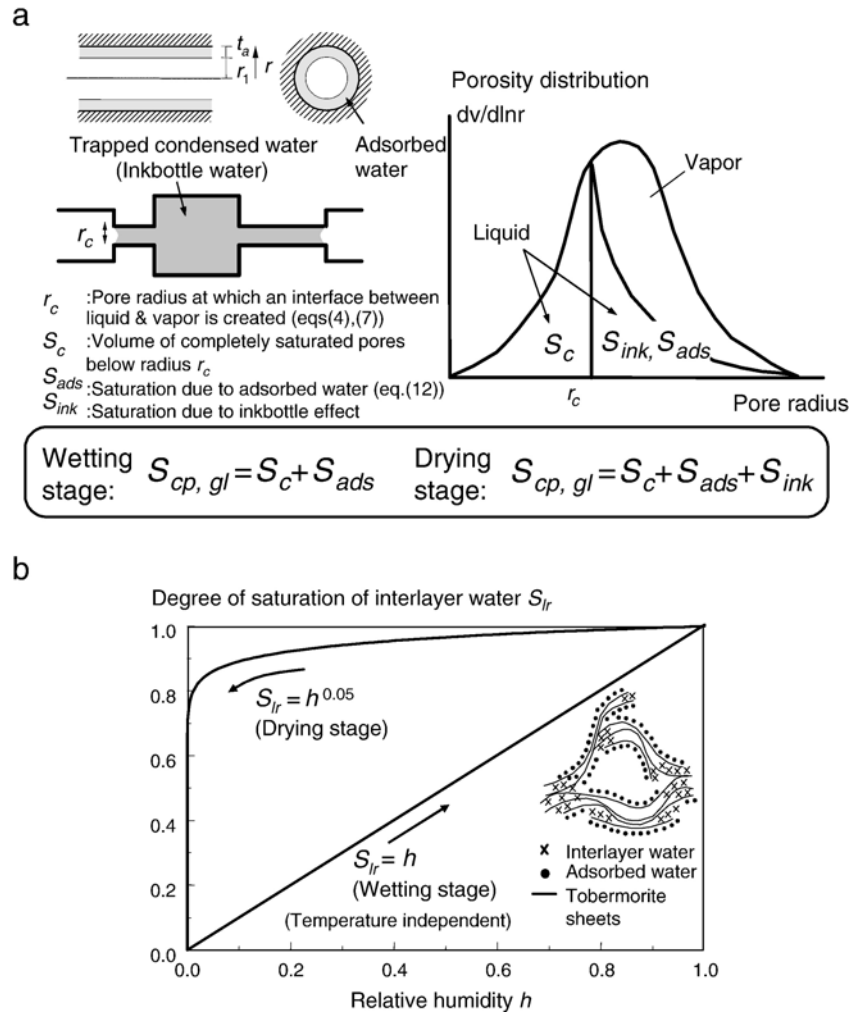Fig. 4. Multi-scale modeling of moisture existing in capillary, gel and interlayer pores.

Fig. 5. a. Thermodynamic moisture equilibrium of condensed and adsorbed water in capillary and gel pores. b. Empirical modeling of moisture isotherm for interlayer water.

condensed water can be determined from r_c derived from the moisture equilibrium equations and the pore distribution function. Then, in order to take into account the contribution of adsorbed water in the unsaturated pores, the degree of saturation S_{ads} is calculated by integrating the adsorbed water layer thickness determined by the B.E.T. theory (Eq. (12)) with respect to the pores. Then, as the sum of the quantities of water thus obtained, the degree of saturation in the wetting phase is calculated (Fig. 5). In the drying phase, the overall degree of saturation is calculated by adding additional moisture S_{ink} due to the inkbottle effect. Moisture isotherms determining the state of interlayer water are expressed by the same functional equations regardless of temperature (Fig. 5). From these physical models, the total degree of saturation S_{total} is calculated as

$$S_{total} = \frac{\phi_{cp} \cdot S_{cp} + \phi_{gl} \cdot S_{gl} + \phi_{lr} \cdot S_{lr}}{\phi_{cp} + \phi_{gl} + \phi_{lr}} \qquad (20)$$

where, ϕ_{cp}: capillary porosity, ϕ_{gl}: gel porosity; ϕ_{lr}: interlayer porosity, S_{cp}: degree of saturation of capillary pores, S_{gl}: degree of saturation of gel pores, and S_{lr}: degree of

saturation of interlayer pores. The pore structure development model [1] gives each of these porosities for arbitrary stage of hydration.

Fig. 6 shows the computed moisture isotherms. As shown, although temperature-dependent surface tension and density are introduced, the computed moisture isotherms at different temperature conditions do not show any significant differences.

Fig. 7 shows moisture loss behaviors under 20 °C and 60 °C. Prismatic mortar specimens (4 × 4 × 16 cm) with a water-to-cement ratio of 50% were prepared. After the specimens were sealed-cured for 38 days, they were dried in a controlled chamber at 60% RH. As shown, moisture loss at normal temperature (20 °C) is accurately predicted, but the calculated values for 60 °C do not capture the actual trends. Although relative humidity in the external environment is 60% RH in both cases, the absolute vapor density gradient $\nabla \rho_v$ at higher temperatures is large because of the temperature dependence of saturated vapor pressure. Consequently, the computed moisture loss behavior in the early stages of drying are high similar to the real behavior, but the continuous moisture loss cannot be seen in the analysis. As shown in Fig. 6, the moisture
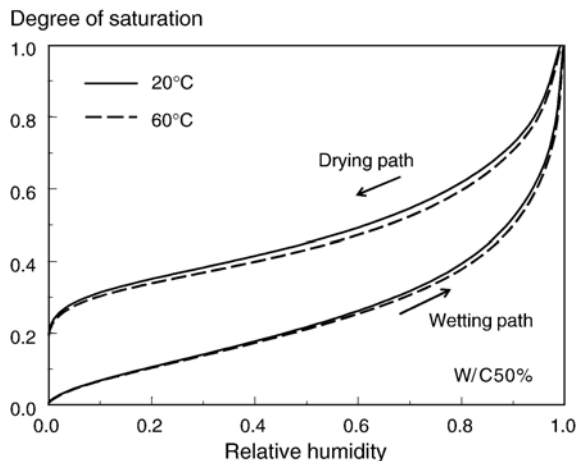
Degree of saturation

Fig. 6. Computed moisture isotherm at 20 °C and 60 °C.

isotherms, which determine the water content of the specimens, do not differ significantly at the two temperatures, so the amount of moisture loss does not show any significant difference.

These results indicate that the most important thing for enhancing the accuracy of overall computation is an appropriate expression of moisture equilibrium based on microscopic viewpoint. In the moisture isotherm model used in the calculation, the effects of temperature for the two-phase equilibrium of condensed liquid and vapor (Eqs. (4) and (9)) and adsorbed water on the pore wall surfaces (B.E.T. theory, Eqs. (12) and (13)) have already been given according to the thermodynamic theory. The hysteresis model based on the hypothesis of the inkbottle effect and the interlayer water model have only been verified through the observed behaviors at room temperature (20 °C). It was tackled, therefore, to extract these temperature effects from the following systematic experiments. The reason is that if an attention is paid only to the total summation of moisture from macroscopic point of view, simple phenomena behind apparently complex behavior might be overlooked.
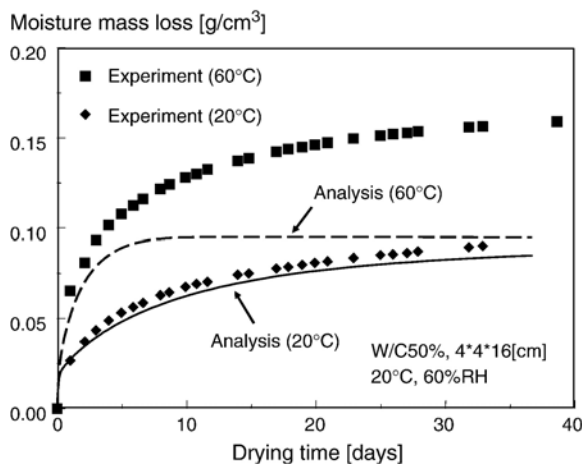
Moisture mass loss [g/cm³]

Fig. 7. Moisture loss behaviors at 20 °C and 60 °C.

3. Temperature effect on internal moisture state in cementitious material

3.1. Test method

3.1.1. Mix proportions, specimen preparation method and curing conditions

Table 1 shows the mix proportions for the test specimens. Cement paste specimens with a water-to-cement ratio of 50% were prepared using ordinary Portland cement. In order to prevent bleeding during setting, 15% or 40% of limestone powder by volume was mixed into the cement paste. In the test, the filler effect of limestone powder did not influence the apparent test results, so hereafter no distinction is made between the two types of mixes in Table 1.

Cylindrical molds used to cast cement paste mixes were 10 cm in diameter and 20 cm in height. Molded cement paste was sealed-cured, and they were removed after one day of curing. Then, in a climate-controlled room kept at 20 °C and 60% RH, the molded cement paste blocks were cut into about-one-centimeter cubes by using a wet-type concrete cutter, and these cubes were water-cured for 80 days at 20 °C. The aim of this method was to ensure the progress of hydration reaction and eliminate the influence of the hydration-induced consumption of free water during wetting–drying testing and changes in pore structure on moisture equilibrium. The specimens were wetted or dried at three temperature levels (20 °C, 40 °C and 60 °C). Before they were used for testing, the specimens were stored for 1 week in water kept at 20 °C, 40 °C or 60 °C.

3.1.2. Method of wetting and drying specimens

After water curing, the specimens were wetted or dried under the conditions shown in Tables 2 and 3 in a climate-controlled chamber capable of controlling both temperature and humidity with high accuracy. During the test period, temperature in the chamber was kept within ± 0.5 °C of the specified level, and relative humidity was kept within ± 2%. The tests were conducted under different temperature and relative humidity conditions for the drying process starting from the complete saturation of the specimen and the wetting process starting from the complete dispersion of liquid water and interlayer water. In this study, an oven-dry condition achieved by 105 °C drying is defined as a zero-saturation state in which neither liquid water nor interlayer water exists.

3.1.3. Separate measurement of liquid water and interlayer water

In order to measure liquid water and interlayer water in the specimens separately, an organic solvent-based water extraction method was used [8]. In the method, internal moisture is leached

Table 1
Mix proportion of cement paste specimen

Water-to-cement ratio (%)	Unit mass (kg/m3)		
	Water	Cement	Lime powder
50	520	1040	405
	367	734	1080

Table 2
Wetting conditions in the experiment

Temperature	Relative humidity	Duration of wetting (days)
20 °C	40%, 55%, 70%, 85%	7
40 °C	40%, 55%, 70%, 85%	7
60 °C	30%, 60%, 90%	7, 14, 28

out by immersing a hardened cementitious material in a hydrophilic organic solvent.

The most important requirement for this test is to properly separate liquid water and interlayer water. A study has pointed out [8], however, that the amount of water that can be leached out varies depending on the type of the solvent used. One possible factor is differences in the size, structure or other attributes of solvent molecules that influence the ability of solvents to leach out water from hardened cementitious materials. The structure of C–S–H gel and the distribution interlayer water and gel water are usually illustrated as in Fig. 5b [9]. In reality, however, there is no clearly discernible boundary, and measured values may vary depending on solubility.

In this study, the authors decided to use ethanol as an organic solvent in view of the results of preliminary tests conducted on methanol, ethanol and propanol. Table 4 shows the test results used as the basis of the decision to use ethanol. In the test, after one-centimeter-thick specimens were cured in water for 3 months, the specimens were immersed in the organic solvent until the water concentration in the solvent reached a state of equilibrium (immersed for 40 days or, only in the cases where the water-to-cement ratio was 25%, for 70 days). Both the curing in water and the immersion in ethanol were carried out at 20 °C. It is likely that after 3 months of water curing, all pores are saturated with liquid water and interlayer water, and that the amount of water can be extracted by the organic solvent is equal to the amount of liquid water existing in the capillary and gel pores. As shown in Table 4, measured values and calculated values of the different water-to-cement ratios designed to vary the capillary, gel, and interlayer water composition show several percent of differences, but they show fair agreement. Thus, the measured values of physical quantities obtained in the test and the calculated values for condensed water obtained from the analysis model can be regarded as mostly in agreement. In this study, therefore, the water that is leached out by ethanol is defined as liquid water (condensed water + adsorbed water) existing in the capillary and gel pores, and the remaining water is defined as interlayer water.

After the specimens were subjected to various wetting and drying conditions, they were immersed in ethanol in sealed containers kept at 20 °C for 40 days, and the amount of water thus extracted was measured with a trace moisture meter using the Karl Fischer titration method. The amount of water thus

Table 3
Drying conditions in the experiment

Temperature	Relative humidity	Duration of drying (days)
20 °C	30%, 60%, 90%	7, 28, 60
40 °C	60%	7, 14, 28
60 °C	30%, 60%, 90%	7, 14, 28, 60

Table 4
Measured and computed values of liquid water existing in capillary and gel pores

	Amount of liquid water (%) (measured)	Amount of liquid water (%) (computed)
Cement paste (W/C65%)	75.7	81.1
Cement paste (W/C50%)	70.0	73.0
Mortar (W/C50%)	72.4	73.0
Cement paste (W/C25%)	57.7	61.5

extracted was taken as the amount of liquid water. The degree of saturation S_{lw}, which is the ratio of the volume of liquid water to the volume of pore space, was calculated using Eq. (21):

$$S_{lw} = \frac{V_{lw}}{V_{lw}^{sat}} \qquad (21)$$

where, V_{lw}^{sat}: volume of liquid water per unit oven-dry mass of specimen at saturation (20 °C) [ml/g], and V_{lw}: volume per unit oven-dry mass of liquid water existing in a specimen subjected to a specified period of drying and wetting [ml/g]. In the test, samples were put into three containers for immersion in ethanol, and the measured values were averaged.

3.2. Behavior of liquid water under different temperature conditions

Figs. 8–10 show the degrees of saturation of liquid water subjected to specified environmental conditions for 7 days. In the wetting process, specimens in an oven-dry condition achieved after 105 °C drying were subjected to different relative humidities. In the drying process, drying was started from the state in which all pores in the specimen were saturated with water. For comparison, calculated values obtained from an analysis model (Fig. 5) are also shown in Figs. 8–10. As the initial conditions and boundary conditions for the analysis, the mix proportions (water-to-cement ratio, volume fraction of aggregate, air content), properties of the materials used (chemical composition of binder, specific gravity, Blaine fineness index, etc.) and curing conditions (boundary conditions for heat and moisture transfer) used in the test were given.
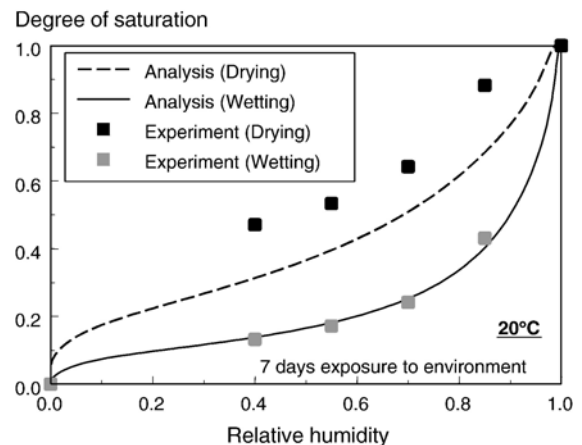
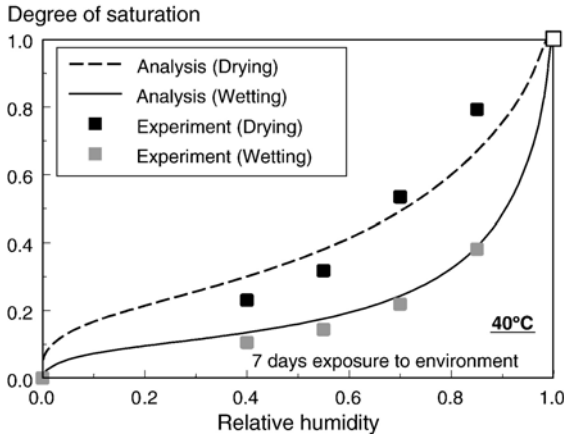

Fig. 8. Moisture isotherm of liquid water at 20 °C.

Fig. 9. Moisture isotherm of liquid water at 40 °C.

For the wetting process, the measured saturation and the calculated values obtained from the analysis model show fair agreement, indicating that the moisture in the hardened cementitious material in the wetting phase is in a state of equilibrium described by the thermodynamic theory. This means that the state of internal moisture can be expressed as the sum of the amounts of condensed water and adsorbed water that can be determined by vapor–liquid equilibrium and the B.E.T. theory (Fig. 5).

The situation differs considerably, however, with respect to the drying phase. As temperature rises, measured values become smaller than calculated values and gradually approach the values in the wetting phase. This tendency is particularly pronounced in the low humidity range. The analysis model tries to explain the moisture hysteresis during drying and wetting by the inkbottle effect [1,2] (Fig. 5). The model takes this approach on the assumption that moisture trapped in inkbottle-shaped pores brings higher water content in the drying phase than that in the wetting phase. One possible cause of the disappearance of hysteresis as temperature rises or as humidity decreases is the stability of moisture trapped in the inkbottle-shaped pores.

The requirement for the third law of thermodynamics dictates that if stability is to be maintained for an infinite period of time, inkbottle-shaped pores in which moisture is trapped must be completely closed spaces. If, however, numerous micro-pores are interconnected in many directions, it is very unlikely that completely closed spaces are formed. It is logical to assume that moisture trapped during the drying process will be gradually dispersed over a long period of time. The rates of transport and dispersion are strongly dependent on temperature. It is reasonable to assume, therefore, that as temperature rises to 40 °C and to 60 °C, the moisture trapped in the inkbottles becomes increasingly subject to transport and diffusion so that the isotherm path in the drying phase gradually becomes closer to that in the wetting phase.

Fig. 11 shows previously reported test results relevant to this discussion [10]. In the reported case, one-millimeter-thick cement paste specimens with a water-to-cement ratio of 50% were prepared by using purely synthetic C_3S, and these specimens were cured for 5.8 years in order to complete the hydration process. Then, the specimens were dried at 25 °C from a saturated condition, and the total water content was measured. As shown in Fig. 11, even in the case of very thin specimens, the water content continues to change for as many as 170 days at normal temperature, indicating that in the drying phase, a long period of time is required before equilibrium is reached.

In order to investigate in detail the time dependence described above, a series of tests was conducted under different temperature conditions for different exposure periods. The test method is as described earlier. Figs. 12–15 show the test results. In the wetting phase (Fig. 12), similar values were obtained regardless of exposure periods, indicating a temporally stable state of equilibrium. Figs. 13–15 show the degrees of saturation of specimens dried at 20 °C, 40 °C and 60 °C. Let us first pay attention to the influence of temperature. Examination of behavior at the relative humidity of 60% reveals that the rate of dispersion during each period increased as temperature rose. In the 60 °C test, the degree of saturation decreased gradually as time passed, and on and after day 28 reached the level of values typically found in the wetting phase, resulting in a state of equilibrium as given by the model. These test results suggest that even the moisture trapped by the inkbottle effect caused by interconnected micro-pores continues to disperse gradually toward the thermodynamic state of equilibrium so as to reach a state of equilibrium similar to that in the wetting phase. From the fact that the degree of saturation decreased quickly as
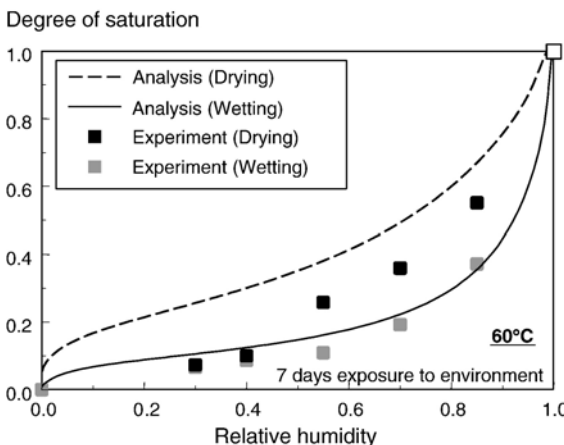

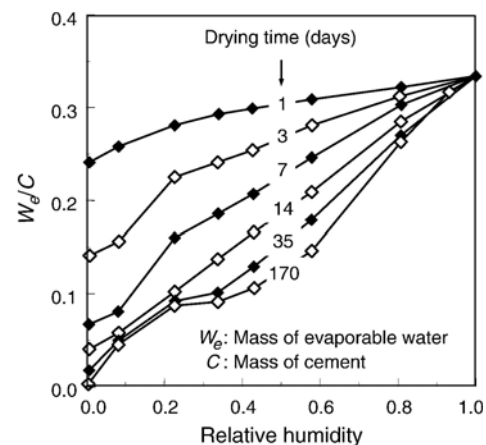Fig. 10. Moisture isotherm of liquid water at 60 °C.

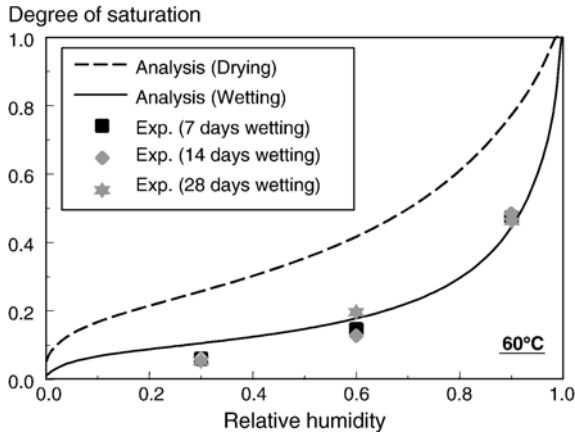Fig. 11. Desorption curves for an initially saturated C_3S paste [10].

Fig. 12. Degree of saturation in the wetting process at 60 °C for different exposure periods (liquid water).
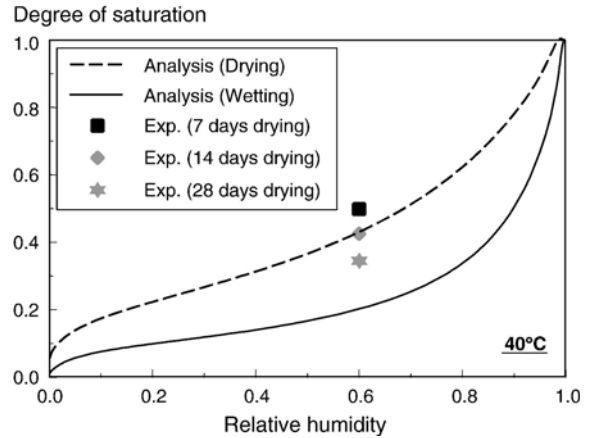

Fig. 14. Degree of saturation in the drying process at 40 °C for different exposure periods (liquid water).

temperature increased, it can be inferred that the dispersion of moisture trapped in inkbottle-shaped pores is strongly related to the chemical potential of internal water molecules.

Next, let us consider the effect of relative humidity. Comparison revealed that under all temperature conditions and for all drying periods, the rate of dispersion increased as relatively humidity decreased. At the temperature of 60 °C, for example, a state of equilibrium was reached on the wetting curve in the 30% and 60% cases while at the relative humidity of 90%, there was a difference between the drying and wetting curves even after 60 days of drying. At the relative humidity of as high as 90%, more pores are in a saturated condition than under other conditions. In a situation like this, there are only limited dispersion paths for the moisture trapped by the inkbottle effect (i.e., a higher likelihood of the formation of completely closed pore spaces).

3.3. Behavior of interlayer water under different temperature conditions

Figs. 16–18 show the relationships between the amount of extracted interlayer water and relative humidity. The amount of

interlayer water was calculated by subtracting the amount of liquid water extracted by the solvent extraction method after 7 days of exposure under different conditions from the total amount of water. The degree of saturation of interlayer water, S_{iw}, was calculated from Eq. (22):

$$S_{iw} = \frac{V_{iw}}{V_{iw}^{sat}} \tag{22}$$

where, V_{iw}^{sat}: volume of interlayer water per unit oven-dry mass of specimen at saturation (20 °C) [ml/g], and V_{iw}: volume of interlayer water per unit oven-dry mass existing in a specimen subjected to specified periods of drying and wetting [ml/g]. In the evaluation of the test results, the amount of interlayer water in saturated condition at 40 °C and 60 °C was not measured; instead, the degree of saturation at 20 °C was taken as a reference value and calculated as shown in Eq. (22). The values calculated under different temperature conditions are relative values based on the saturated condition at 20 °C.

In this study, the amount of interlayer water in the specimens subjected to up to 60 days of wetting and drying, as well as 7 days of exposure, was measured. The specimens, however,
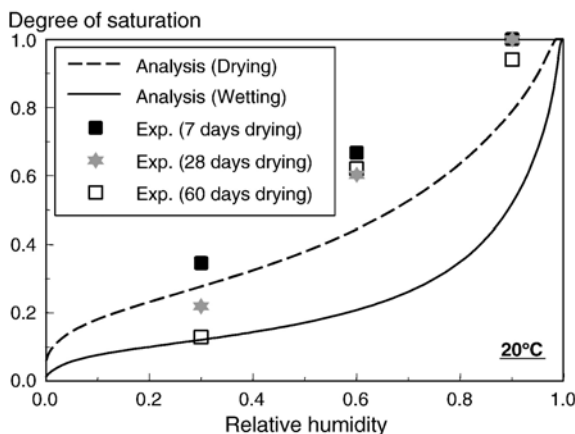

Fig. 13. Degree of saturation in the drying process at 20 °C for different exposure periods (liquid water).
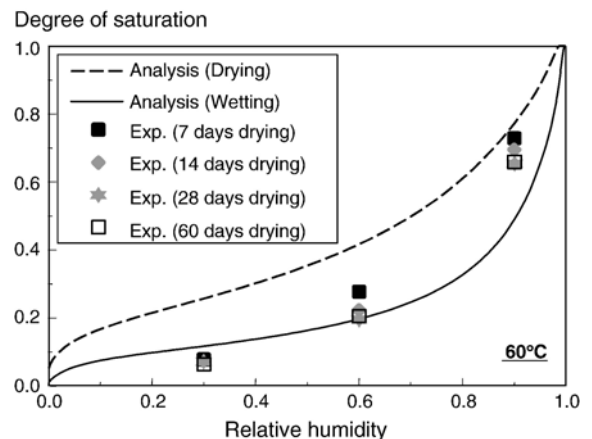

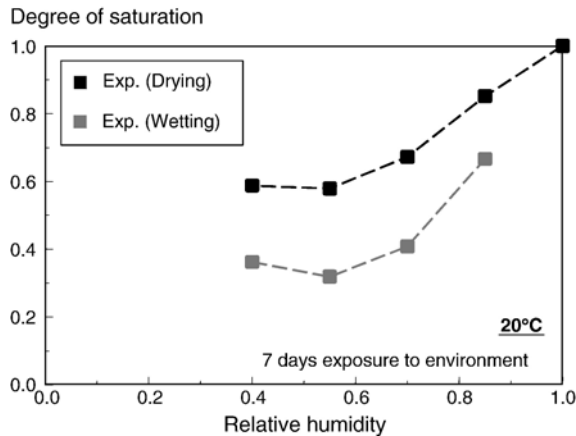Fig. 15. Degree of saturation in the drying process at 60 °C for different exposure periods (liquid water).

Fig. 16. Degree of saturation at 20 °C (interlayer water).

Fig. 18. Degree of saturation at 60 °C (interlayer water).

exposed to a high temperature (60 °C) and a medium relative humidity (60% RH) showed increases in the mass of the specimen, particularly after 28 days. Thermal gravimetric analysis (TGA) revealed the production of calcium carbonate, suggesting the possibility of mass increases due to carbonation. Eliminating the influence of carbonation is important because the amount of interlayer water is measured by measuring the total mass of the specimen and then subtracting the mass of moisture extracted by the solvent extraction method. In this study, only data that did not indicate the production of calcium carbonate were chosen in advance through TGA test.

One thing worthy of note about the test results is that the apparent behavior of interlayer water does not indicate the influence of the drying–wetting hysteresis at 40 °C or 60 °C. Another thing worthy of note is that the degree of saturation is more or less constant regardless of relative humidity. For example, the measured degrees of saturation of interlayer water ranged from 30 to 40%. These values indicate the ratio of the amount of interlayer water stably existing at 20 °C to the measured amount of interlayer water in a saturated condition at the same temperature. The amount of moisture in a stable state varied with temperature. At 20 °C, there are path differences between the drying phase and the wetting phase. A certain amount of time is required in order for
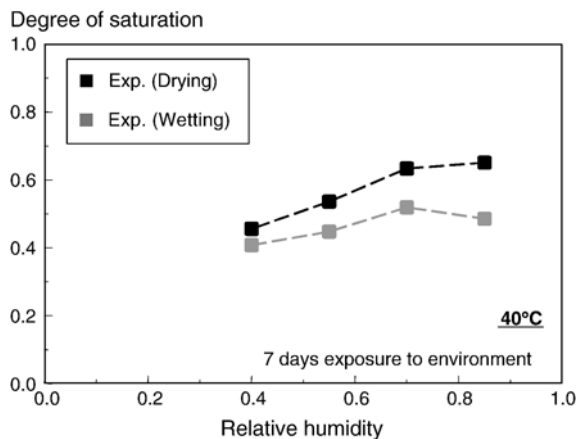
interlayer water to recover from an oven-dry condition [11]. Part of interlayer water, therefore, did not reach a state of equilibrium after 7 days of wetting, and it can be inferred that the degree of saturation in the wetting phase was undermeasured under the time conditions used in the test.

4. Generalized model for moisture equilibrium

4.1. Condensed liquid water

The discussion described in the preceding chapters have confirmed that the test results concerning the wetting phase show good agreement with the total amount of liquid water calculated as the sum of the amounts of condensed water and adsorbed water expressed by the Kelvin's equation and the B.E.T. theory. In the drying phase, however, behavior varies considerably depending on the temperature and humidity to which the specimen is exposed. There is a difference in the time elapsed before reaching the equilibrium depending on temperature and humidity, but it can be assumed that ultimately the relationship between the degree of saturation in the drying phase and relative humidity follows the equilibrium curve for the wetting phase.

The inkbottle effect has been already mentioned as a cause of the short-term drying–wetting hysteresis. That is, the requirement for the third law of thermodynamics dictates that water trapped in the "inkbottles" can exist only in closed spaces. The probability of occurrence of completely closed spaces in an irregular and complex pore structure is low. It can be inferred that the moisture trapped by the inkbottle effect will gradually disperse into adjacent connected pores at the rates corresponding to ambient temperature and relative humidity. This section proposes a model that expresses the process of the transition to moisture equilibrium in the drying phase.

A relatively short-term monotonic drying process at normal temperature, though depending on the size of the object to be analyzed, has been accurately modeled as follows (Fig. 5) [1,2]:

Fig. 17. Degree of saturation at 40 °C (interlayer water).

$$S = S_c + S_{ads} + S_{ink} \tag{23}$$

where, S: degree of saturation with condensed water and adsorbed water, S_c: degree of saturation with moisture existing in pores below radius r_c, S_{ads}: degree of saturation due to adsorbed water, and S_{ink}: degree of saturation with trapped water due to the inkbottle effect. As is evident from the discussion so far, the model can be enhanced overall by introducing the influence of temperature on the degree of saturation associated with the inkbottle effect. With the aim of taking into account the time-dependent dispersion of "inkbottle water," it was decided to incorporate the effect of temperature in the simplest form while following the basic principles of the existing model.

$$S = S_c + S_{ads} + k \cdot S_{ink} (0 \leq k \leq 1) \tag{24}$$

where k is a parameter that takes the value of 1.0 immediately after the start of the drying process and decreases with the progress of drying (Fig. 19. When the wetting curve is reached after the passage of sufficient time, k takes the value of zero. As indicated by the test results shown in the preceding chapter, the rate of decrease of this parameter is dependent on temperature and is also influenced by ambient humidity. Since Eq. (24) is a model that describes local equilibrium in pores, results obtained specimens of finite dimensions (one-centimeter cubes) cannot be taken as the properties of infinitesimal volume elements. The only logical way to directly determine the properties of infinitesimal volume elements is to conduct tests on infinitesimal volume specimens. For this reason, sensitivity to temperature and humidity was back-analyzed through finite element analysis consistent with the test conditions. To be more specific, a one-centimeter mesh was prepared, temperature and humidity conditions identical to the test conditions were given as conditions for analysis, and parameters were determined so that the averages of the calculated values within the finite dimensions were consistent with the macroscopic test results shown earlier (Figs. 13–15). As a result, the following equation was obtained:

$$\frac{dk}{dt} = -C \cdot a_{ink}^T \cdot a_{ink}^h \cdot k$$
$$a_{ink}^T = \exp\left(-1.5 \times 10^4 / T\right) \tag{25}$$
$$a_{ink}^h = 0.05 \cdot (100.0 - 100.0 \cdot h)^{0.81}$$

where, C: a constant (3.0×10^{13} [1/s]), a_{ink}^T: coefficient expressing the sensitivity to temperature, a_{ink}^h: coefficient expressing the sensitivity to relative humidity, T: temperature
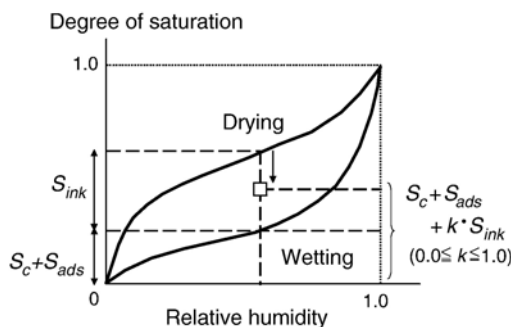

Fig. 19. Enhanced moisture isotherm model considering the time-dependent dispersion of "inkbottle water".
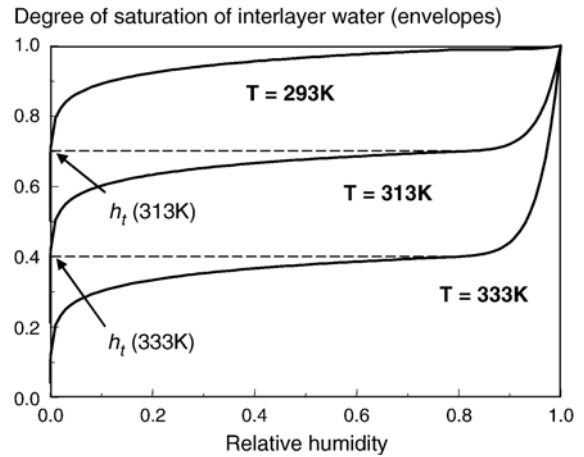

Fig. 20. Moisture isotherm model of interlayer water under different temperature conditions.

[K], and h: relative humidity. In this study, the model expressed by Eq. (25) is proposed as a first step on the basis of the observed facts concerning the water content obtained under limited conditions. This may be considered to correspond to a viscosity term (delayed elasticity term) often used in constitutive equations for visco-elasticity. While working to propose this model, currently the authors are also conducting a study on interdependence between hydration reaction and pore structure development [12] and trying to enhance multi-scale constitutive equations [13] based on thermodynamic state quantities. Taking into consideration these phenomena closely related to the state of internal moisture, the authors will continue a comprehensive study for modeling accuracy enhancement and expand the scope of application by stages.

4.2. Interlayer water

The analysis system uses an empirical model [1,2] of the hysteretic behavior of interlayer water. In order to expand the scope of application to cover a wider range of temperature conditions, it is necessary to take into account the temperature
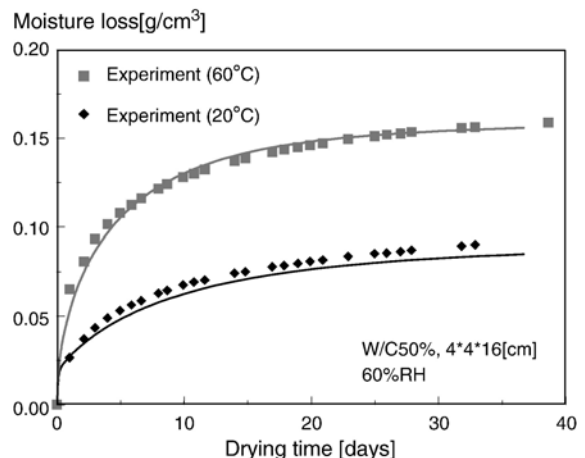

Fig. 21. Computed and measured moisture loss behaviors under different temperature conditions (W/C50% case).
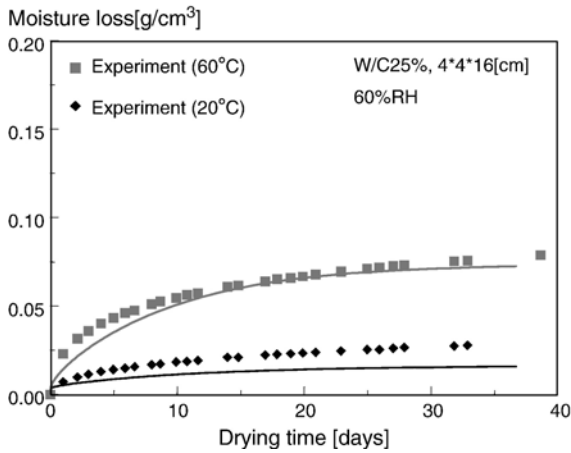
Fig. 22. Computed and measured moisture loss behaviors under different temperature conditions (W/C25% case).

dependence of the equilibrium of not only liquid water but also interlayer water. Thus, the authors introduce a function for expressing an envelope curve on moisture isotherm of interlayer water (Fig. 20), whereas the conventional model assumed a constant temperature of 20 °C.

$$
\begin{aligned}
S_{lr}^{env} &= \frac{a \cdot h^{n_2} + b \, (h \geq 0.8)}{h^{n_1} + c \quad (h < 0.8)} \\
a &= \frac{1.0 - h_t^{env}}{1.0 - 0.8^{n_1}}, \quad b = \frac{-0.8^{n_2} - h_t^{env}}{1.0 - 0.8^{n_1}} \\
c &= h_t^{env} - 0.8^{n_2}, \quad h_t^{env} = -1.5 \times 10^{-2} \cdot T + 5.4 \\
n_1 &= 25.0, \quad n_2 = 0.05
\end{aligned}
\tag{26}
$$

In the above equation, the temperature dependence of interlayer water S_{tr}^{env} is expressed with the parameter h_t^{env}, which shows the ratio of interlayer water existing in a stable condition as a criterion for a saturated state at 20 °C. For 20 °C, parameter values consistent with the existing model shown in Fig. 5 [1,2] were given; for 40 °C and 60 °C, parameters were determined according to the test results reported in the above (Figs. 17 and 18). As Eq. (26) indicates, the model expresses the
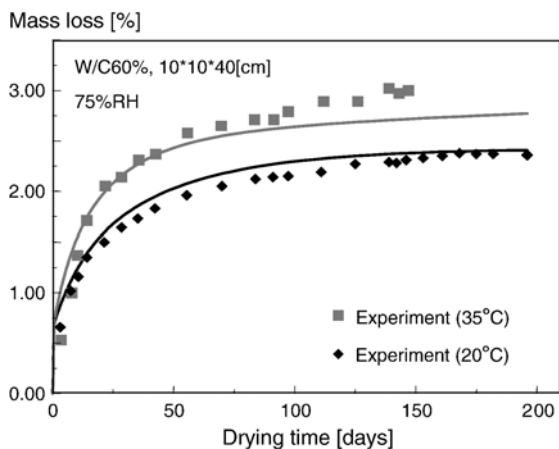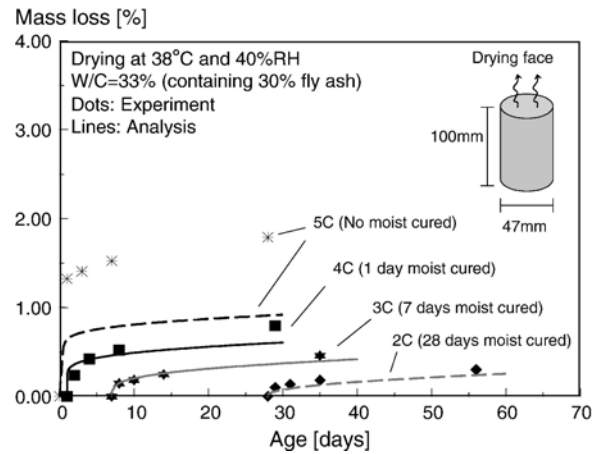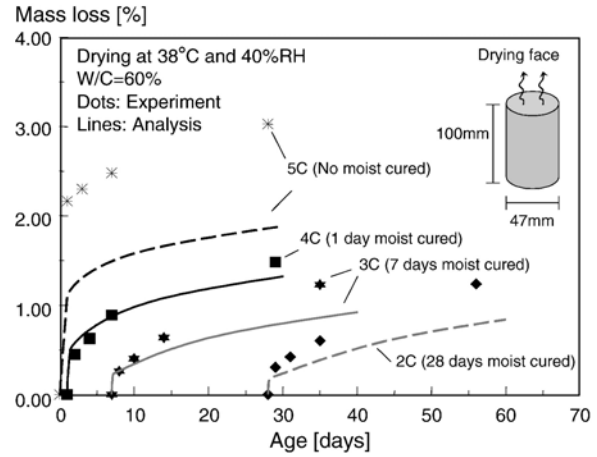

Fig. 24. Computed and measured moisture loss behaviors at high temperature under different curing conditions (Cano-Barrita et al. [15]).

tendency of interlayer water to reach a stable range when humidity reaches 80% and then disappear gradually.

The measured values for interlayer water at 20 °C in the drying phase are smaller than the values given by the proposed model. In the test, water extracted by the solvent extraction method was defined as liquid water, and the difference between

Fig. 23. Computed and measured moisture loss behaviors under different temperature conditions (Ayano and Sakata [14]).
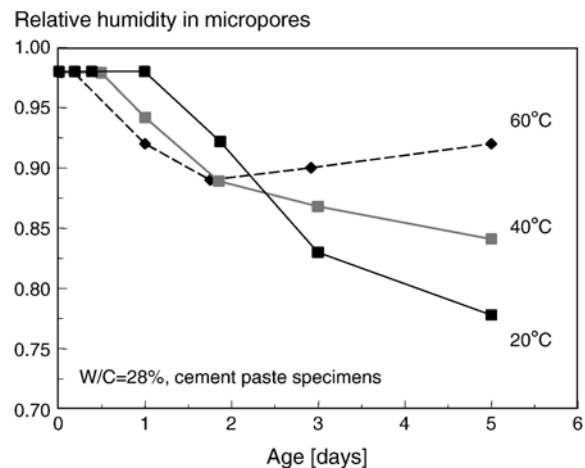

Fig. 25. Measured humidity change under sealed conditions for different temperature conditions (Park and Noguchi [16]).
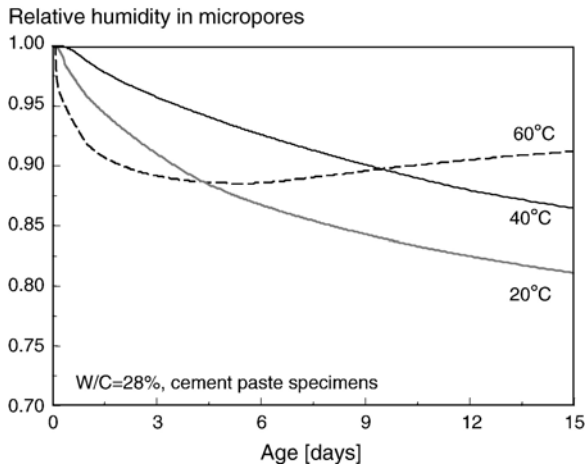
Fig. 26. Computed humidity change under sealed conditions for different temperature conditions.

the total amount of water and the amount of liquid water was taken as the amount of interlayer water. However, the possibility cannot be denied that the values for the components isolated by solvent extraction differ from the definitions used in the analysis. As the reason for this, there is no denying the possibility that the ethanol that has seeped into unsaturated pores after the completion of the normal-temperature drying process extracts part of interlayer water, particularly the kind of interlayer water that would disperse at 40 °C or 60 °C. The authors think that there is a need for further discussion on differences in the solvating ability of different solvents and the amount of bound water that can be extracted, as well as discussion on micro-pore structure change after solvent extraction.

5. Analysis using the proposed model

5.1. Moisture loss behavior

Firstly, moisture loss behavior at different temperatures was studied. The test results shown in Fig. 7 have been analyzed by using the newly proposed model. The dimensions of the specimens and the curing and testing conditions are as described earlier. Figs. 21 and Fig. 22 show calculated moisture loss behaviors of mortar specimens with water-to-cement ratios of 50% and 25%. In both cases, the specimens were dried at a relative humidity of 60%. As shown, the proposed model cap-

tured moisture loss behavior accurately under different temperature conditions.

Fig. 23 shows moisture loss behaviors at 20 °C and 35 °C [14]. Prismatic mortar specimens ($10 \times 10 \times 40$ cm) with a water-to-cement ratio of 50% were prepared. After 14 days of water curing, specimens were dried at 75% RH. As shown, reasonable agreement can be seen for both temperature conditions.

Fig. 24 shows moisture loss of concrete drying at 38 °C and 40% relative humidity [15]. Prior to drying, different curing conditions were given to cylindrical specimens having one exposure surface: 5C (no moist curing), 4C (moist curing for 1 day), 3C (moist curing for 7 days), and 2C (moist curing for 28 days). The proposed model reasonably reproduces moisture loss behaviors for 2C, 3C, and 4C cases, whereas it underestimates the amount of mass loss for 5C. In case of no moist curing, moisture evaporation at the surface is much accelerated, which leads to delay of hydration and increased cracking due to shrinkage. Larger moisture loss measured in the 5C case may be caused by such cracks at the exposure surface, which is not taken into account in the numerical model.

5.2. Interdependence between internal relative humidity and the progress of hydration

Next, the progress of self-desiccation in different thermal environments was investigated. This section focuses on the interdependence among hydration process under sealed condition, temperature and humidity in pores, and the moisture state inside the material. In the test [16], decreases in humidity in pores due to self-desiccation were measured at three temperatures (20 °C, 40 °C, 60 °C). The measuring ranges of the hygrometer used was 0–100 °C and 15–95%, and its accuracy was ± 1 °C and ± 3% RH. In this study, changes in relative humidity of cement paste with a water-to-cement ratio of 28%, made by using ordinary Portland cement, are considered as an example. Generally, hydration reaction at early ages is promoted as curing temperature rises. In fact, in the test conducted by Park and Noguchi [16], the amount of calcium hydroxide generated by hydration reaction increased as curing temperature rose. The degree of self-desiccation, however, did not have a one-to-one relationship with curing temperature or the degree of hydration. At the highest temperature of 60 °C, relative humidity decreased considerably at early stages, but it began to increase at a certain point in time (Fig. 25 [16]).
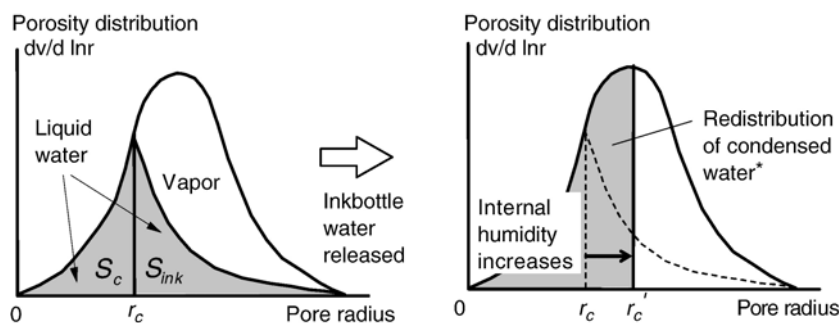

Fig. 27. Schematic representation of redistribution of trapped inkbottle water and increase in relative humidity at high temperature.

A possible mechanism by which relative humidity rose in a 60 °C environment is the temperature dependence of moisture stability. Fig. 26 shows the analysis results. As in the test, relative humidity first decreased to 90% because of hydration reaction at the early stages, but then it increased gradually. The analysis reproduced a tendency obviously differing from the tendency of humidity changes at 20 °C characterized by a monotonic decrease with the progress of hydration. At higher temperatures, water in the inkbottle spaces was released and redistributed as condensed water with the passage of time (Fig. 27). This is why internal relative humidity rose. The analysis simulated the trends of relative humidity with fair accuracy, but there are small differences between the test and the analysis during the periods of increase and decrease. In order to simulate real phenomena accurately and quantitatively, it is necessary to accurately quantify interdependent factors such as early hydration reaction, water consumption, pore structure development, and water equilibrium and redistribution. This is one of the subjects for future research.

6. Conclusion

This study has proposed a model for predicting moisture transport and water content at arbitrary temperature conditions developed by enhancing an existing model. The equilibrium relationship among pore pressure, saturated vapor pressure and absolute vapor pressure has been described by considering the Gibbs energy balance in the vapor and liquid phases, and the flux of vapor and liquid water has been generalized with respect to temperature.

Since moisture existing in hardened cementitious materials can have different levels of temperature and humidity sensitivity depending on the dimensions of micro-pores in which moisture is stored, condensed liquid water and interlayer water were separately extracted by the organic solvent method to quantify their time-dependent stability. As a result, it has been found that the amount of condensed water in the wetting phase under arbitrary temperature conditions can be explained by classical thermodynamics, and that condensed water in such a condition is in a stable state of equilibrium. It has also been found that the hysteresis in the drying phase tends to disappear when exposed to high temperatures, and that the water content in the drying phase that seems to be stable at 20 °C gradually approaches the equilibrium curve for the wetting phase as temperature rises.

As an interpretation of the disappearance of the hysteresis indicated by moisture isotherms, it has been hypothesized that additional moisture trapped by the inkbottle effect gradually disperse because of thermodynamic instability. Interlayer water did not show hysteresis of the drying–wetting cycles. It has therefore been shown experimentally that ambient temperature is the primary governing factor for moisture stability. On the basis of these experimentally verified facts, minimum modifications have been made to an existing model in order to expand the relationship between the water content and internal

relative humidity of hardened cementitious materials for application to arbitrary temperature conditions.

It has also been shown that an analysis using the proposed model can simulate moisture loss behavior under varying temperature conditions and autogenous shrinkage in a closed system. However, although the proposed model, as a means of a first approximation, greatly improves overall system accuracy and applicability, it is still not capable of accurately quantifying the behavior of moisture components. The authors intend to continue to conduct studies on the proposed methodology and at the same time conduct multi-faceted and comprehensive studies through various verifications, such as interrelationship among shrinkage, creep, hydration reaction, pore structure development, and moisture state in cementitious materials.

References

[1] K. Maekawa, R.P. Chaube, T. Kishi, Modelling of Concrete Performance, E and FN SPON, 1999.

[2] T. Ishida, R.P. Chaube, T. Kishi, K. Maekawa, Modeling of pore water content in concrete under generic drying–wetting conditions, Concrete Library of JSCE 31 (1998) 275–288.

[3] K. Maekawa, T. Ishida, T. Kishi, Multi-scale modeling of concrete performance—integrated material and structural mechanics, Journal of Advanced Concrete Technology 1 (2) (2003) 91–126.

[4] Science Handbook, Maruzen, 2002.

[5] A. Hillerborg, A modified adsorption theory, Cement and Concrete Research (15) (1985) 809–816.

[6] J.R. Welty, C.E. Wicks, R.E. Wilson, Fundamentals of Momentum, Heat, and Mass Transfer, John Wiley and Sons, Inc., 1969.

[7] I. Soroka, Portland Cement, Paste and Concrete, Chemical Pub Co, 1980.

[8] K. Fujii, W. Kondo, Kinetics of the hydration of tricalcium silicate, Journal of the American Ceramic Society 57 (11) (1974) 492–497.

[9] R.F. Feldman, P.J. Sereda, A model for hydrated Portland cement paste as deduced from sorption-length change and mechanical properties, Material Construction 1 (6) (1968) 509–519.

[10] H.F.W. Taylor, Cement Chemistry, 2nd ed., 1997 (245 pp.).

[11] S. Asamoto, T. Ishida, Influence of liquid characteristic and its distribution in micro-pore on time-dependent mechanical behavior of concrete, Advances in Cement and Concrete, Proceedings of a Conference Held at Copper Mountain, Colorado, 2003, pp. 181–190.

[12] K. Nakarai, T. Ishida, T. Kishi, K. Maekawa, Enhanced thermodynamics analysis coupled with temperature-dependent microstructures of cement hydrates, Cem. Concr. Res., Monte Verita Conference special issue (in press), doi:10.1016/j.cemconres.2006.10.006.

[13] S. Asamoto, T. Ishida, K. Maekawa, Time-dependent constitutive model of solidifying concrete based on thermodynamic state of moisture in fine pores, Journal of Advanced Concrete Technology 4 (2) (2006) 301–323.

[14] K. Ayano, K. Sakata, Concrete shrinkage strain under the actual atmosphere, Proceedings of the JCI 19 (1) (1997) 709–714.

[15] P.F. de J. Cano-Barrita, B.J. Balcom, T.W. Bremner, M.B. MacMillan, W.S. Langley, Moisture distribution in drying ordinary and high performance concrete cured in a simulated hot dry climate, Materials and Structures 37 (2004) 522–531 (Oct.).

[16] K.B. Park, T. Noguchi, Autogenous shrinkage of cement paste hydrated at different temperatures: influence of microstructure and relative humidity change, in: B. Persson, G. Fagerlund (Eds.), Proc. of the 3rd Int'l Res. Sem., Self-desiccation and Its Importance in Concrete Technology, Sweden, Lund, 2002, pp. 93–101.